Journal of the Mechanics and Physics of Solids 122 (2019) 418–434

Contents lists available at ScienceDirect

Journal of the Mechanics and Physics of Solids

journal homepage: www.elsevier.com/locate/jmps

Mechanical behavior of cross-linked random fiber networks with inter-fiber adhesion

V. Negi, R.C. Picu*

Department of Mechanical, Aerospace and Nuclear Engineering, Rensselaer Polytechnic Institute, Troy, NY 12180, USA

ARTICLE INFO

Article history:
Received 7 June 2018
Revised 2 September 2018
Accepted 21 September 2018
Available online 22 September 2018

Keywords:
Random fiber networks
Adhesive interactions
Mechanical behavior

ABSTRACT

We study the effect of inter-fiber adhesion on the mechanical behavior of cross-linked random fiber networks in two dimensions. To this end, we consider networks with connectivity number, z, below, at, and above the isostaticity limit of the structure without adhesion, z_c. Fibers store energy in the axial and bending deformation mode and the cross-links are of freely rotating type. Adhesive forces lead to fiber bundling and to a reduction of the total volume of the network. The degree of shrinkage is determined as a function of the strength of adhesion and network parameters. The mechanical response of these structures is further studied in uniaxial tension and compression. The stress-strain curves of networks without inter-fiber adhesion exhibit an initial linear regime, followed by strain stiffening in tension and strain softening and strain localization in compression. In presence of adhesion, the response becomes more complex. The initial linear regime persists, with the effective modulus decreasing and increasing with increasing adhesion in cases with $z > z_c$ and $z < z_c$, respectively. The strain range of the linear regime increases significantly with increasing adhesion. Networks with $z > z_c$ subjected to tension strain-stiffen at rates that depend on the adhesion strength, but eventually enter a large strain/stress regime in which the response is independent of this parameter. Networks with $z < z_c$ are stabilized by adhesion in the unloaded state. Beyond the initial linear regime their tangent modulus gradually decreases, only to increase again at large strains. Adhesive interactions lead to similar effects in compression. Specifically, in the $z > z_c$ case, increasing the adhesion strength reduces the linear elastic modulus and significantly increases the range of the linear regime, delaying strain localization. This first investigation of the mechanics of cross-linked random networks with inter-fiber adhesion opens the door to the design of soft materials with novel properties.

1. Introduction

Many materials of everyday use are made from fibers or have a fiber network as their main structural component. Building three-dimensional constructs from filaments increases the effectiveness of material use, reducing material consumption and leading to lightweight products. This is extensively exploited in the biological world where most materials are fibrous. Collagen and elastin fibers form all connective tissues and membranes in animal bodies, the structural component of eukaryotic cells – the cytoskeleton – is a complex network of protein filaments, plant stems are fibrous, and fungi grow by extending tubular filaments called hyphae.

* Corresponding author.
E-mail address: picuc@rpi.edu (R.C. Picu).

https://doi.org/10.1016/j.jmps.2018.09.027
0022-5096/

Engineered fibrous materials include non-wovens as well as various types of woven structures such as cloth, tissue, filters, insulation, etc. Molecular networks, such as gels and rubber, are also widely used. These are usually soft materials that accommodate large deformations and exhibit high toughness (Darnell et al., 2013; Erman and Mark, 1997).

Interactions in fiber networks are of bonded and non-bonded type. In bonded networks, inter-fiber bonds engage the axial, bending and torsional deformation modes of fibers. Topological interactions, associated with the condition that fibers do not cross or overlap, are of non-bonded type and become important in compression, under large deformations, in both bonded and non-bonded networks (Picu and Subramanian, 2011; Toll, 1998).

Fibers can also interact adhesively, which leads to fiber bundling. Adhesive interactions may originate from various sources such as hydrophobic attraction between filaments, hydrogen bonding, electrostatic interactions, etc, each being dominant in specific material systems. Adhesion forces are short-ranged, and fibers must be brought in close contact by other agents for adhesion to become active. Examples include 'mechanical activation' of non-wovens which is known to increase their stiffness and strength (Linares et al., 2009), and elastocapillarity which organizes fibrous assemblies into bundles (De Volder and Hart, 2013). Capillarity may be used to produce a variety of effects in soft matter, as reviewed in (Style et al., 2017). In all cases, capillary forces bring elastic structures (fibers or foils) in contact, after which these are held together by adhesive forces. Suspensions of rigid and flexible fibers undergo flocculation as the concentration increases. The formation of filament bundles was observed in dense suspensions of actin (Tempel et al., 1996) and collagen (Yunoki et al., 2015) and the process was discussed theoretically by Zilman and Safran (2003).

The effect of adhesion can be evaluated in terms of the elastocapillary length $L_{\mathrm{EC}} = \sqrt{E_f I/\gamma}$ (Bico et al., 2004), which captures the physics of bending-dominated elasticity in presence of surface forces (Israelachvili, 2011). The parameters E_f and I are the elastic modulus of the fiber material and the moment of inertia of the fiber cross-section, while γ represents the work of adhesion per unit length of contact between two fibers with parallel axes. Adhesion becomes important when L_{EC} is comparable to other characteristic lengths of the fibrous structure, such as the fiber length, L_0, or the mean segment length of the fiber network (i.e. the mean distance between two cross-links along given fiber), l_c (Picu and Sengab, 2018). L_{EC} for PAN nanofibers of diameter 300 nm is approximately 34 μm, $L_{\mathrm{EC}} = 10$ nm for single-walled CNT (10,10) of diameter 1.4 nm, and 7 μm to 20 μm for microtubules (Picu and Sengab, 2018). For actin filaments, having $E_f I = 7.3 \times 10^{-26}$ N m^2 (Gittes et al., 1993) and effective $\gamma \sim 0.40 \pm 0.188$ pN (Streichfuss et al., 2011) in the presence of Mg^{2+} ions, L_{EC} takes values in the range 0.35 μm to 0.59 μm. L_{EC} was used to rationalize the adhesion-driven organization of carbon nanotubes in buckypaper and formation of nanotube bundles (Berhan et al., 2004; Coleman et al., 2003; Liu et al., 1998; Lu, 1997). The size and structure of bundles depends on the bending stiffness (i.e. whether the buckypaper contains single wall or multiwall CNTs) and the length of filaments.

A detailed analysis of the structural organization driven by adhesive forces in non-bonded fiber assemblies was presented in (Picu and Sengab, 2018). The non-dimensional parameters that control the evolution of the structure are ρL_0, where L_0 is the fiber length and ρ is the network density (total length of fibers per unit area of the fiber mat), and $\Psi = (L_0/L_{\mathrm{EC}})^2$. It was shown that the fibrous system evolves when $\Psi > a(\rho L_0)^2$, where a is a numerical parameter, and remains in the as-deposited state when this condition is not fulfilled. Further, evolving structures may disintegrate into isolated bundles at small values of ρL_0, while a cellular network of fiber bundles forms at larger ρL_0. The boundary between non-evolving and evolving network states depends on the presence and the magnitude of friction between fibers (Sengab and Picu, 2018). Friction leads to an increase of parameter a and extends the range of non-evolving structures to larger values of Ψ.

Substantial work was dedicated to the mechanics of cross-linked networks of fibers both in the mechanics of materials and physics literature (see reviews (Broedersz and MacKintosh, 2014; Picu, 2011)). Generically, networks without adhesive interactions subjected to either uniaxial tension or shear exhibit three regimes: a linear elastic response at small strains, followed by strain stiffening at intermediate strains, and by a third linear regime at even larger strains. Network deformation is generally non-affine, with the local strains being different from the applied far-field strain and varying with the position in the network. A transition from quasi-affine deformation, observed at high network densities, ρ, and when fibers are stiff in bending (large $E_f I$), to strongly non-affine deformation at low ρ and $E_f I$ was reported (Head et al., 2003). In non-affine conditions, the small strain modulus of the network, E_0, varies linearly with $\rho^x E_f I$, where the exponent x depends on the network architecture and embedding space dimensionality (Heussinger and Frey, 2007; Islam and Picu, 2018; Shahsavari and Picu, 2013). This relation becomes $E_0 \sim \rho E_f A$ in affine conditions, where A is the cross-sectional area of fibers. Beyond the first linear elastic regime, networks strain-stiffen either exponentially or as a power function of strain. The type of stiffening depends on the network architecture (Islam and Picu, 2018). Exponential stiffening is broadly reported in the biomechanics literature related to soft tissue mechanics (Fung, 1993). During this process, fibers gradually orient in the loading direction and the network becomes mechanically anisotropic. When fiber orientation ceases, the load is transmitted exclusively along 'stress paths' that percolate across the sample and the stress-strain curve enters the third linear elastic regime.

In compression, networks also exhibit three regimes. The first regime is linear elastic and the effective modulus in compression is identical to that measured in tension. A gradual reduction of the tangent modulus is observed at intermediate strains. Similar to the compressive behavior of cellular materials (Gibson and Ashby, 1999), this is associated with strain localization. However, the more disordered structure of random fiber networks prevents localization in a narrow band, as usually observed in the cellular case. The segment of the strain-strain curve corresponding to this localization regime has positive slope, with the tangent stiffness increasing with increasing the degree of structural disorder of the network. Pronounced strain stiffening is observed at larger strains, which is due to the formation of contacts between fiber segments. This regime is well described by the model proposed by Toll (1998).

While the mechanical behavior of bonded networks without adhesion is, in general terms, well understood, the effect of adhesion on the mechanics of such structures has not been explored to date. This article is devoted to the investigation of this effect. The studies discussed above related to the effect of adhesion on non-bonded network mechanics (Picu and Sengab, 2018; Sengab and Picu, 2018) indicated that adhesion may significantly re-organize the network. Such re-organization is expected to also occur in the case of bonded networks, although its extent should be limited due to the constraints imposed by the bonds. To clarify this aspect, we study first the network re-organization and observe significant, Ψ-dependent shrinkage under the action of inter-fiber adhesion. Further, we study the mechanical behavior of these structures in tension and compression. To preserve simplicity, in this first study of such systems we consider two-dimensional (2D) networks. However, the trends observed are expected to be more generally applicable to three-dimensional networks and to architectures other than those considered here. We observe that adhesion modifies substantially the mechanics of the network, significantly modifying the effective small-strain stiffness, drastically increasing the range of the linear elastic response, postponing strain localization in compression, and even leading to a regime in which the tangent modulus decreases with increasing strain in uniaxial tension.

2. Models and methods

2.1. Models

We consider models in which fibers are made from the same linear elastic material of Young's modulus, E_f, and have identical cross-sectional area, A, and moment of inertia, I. The cross-section and bending rigidity are considered sufficiently large for fibers to be athermal and behave as beams. Inter-fiber adhesion is defined by the energy gain per unit area of contact when two surfaces are brought together, γ_0. In the case of cylindrical filaments, the contact is established over an area of width c_0. In absence of chirality, the two cylinders in contact remain parallel. The Johnson-Kendall-Roberts (JKR) and the Derjaguin-Muller-Toporov (DMT) theories predict that $c_0 \sim (\gamma_0 A/E_0)^{1/3}$ (Derjaguin et al., 1994; Johnson, 1985; Persson, 2006). The adhesion energy per unit length of filament contact, or the work of separation, is $\gamma = \gamma_0 c_0$ (Schmied et al., 2012).

Since the range of adhesive forces is small compared with the other length scales of the problem, we take here an energetic view similar to that used in the JKR theory (Johnson et al., 1971). This allows us to avoid accounting explicitly for the effect of adhesion forces in system dynamics. In contact mechanics, the validity of this approach is determined by the Tabor parameter (Tabor, 1977), $(R\gamma^2/E^2q^3)^{1/3}$, where R and E are the equivalent radius of curvature and the equivalent modulus of the two surfaces in contact, and q is a parameter proportional to the range of the adhesive forces. The JKR theory is found to be applicable only for high values of the Tabor parameter. This approximation is used in the present representation of the inter-fiber contacts.

We consider here 2D networks of Delaunay (DN) and Voronoi (VN) type, Fig. 1(a) and 1(b). Periodic networks are generated by performing the respective tessellation using a set of randomly distributed points in 2D. These points are repeated in plane using periodic lengths $\lambda_x = \lambda_y = L$ in the two in-plane directions, which defines the model size. In such structures, fibers have two cross-links at the two ends. The length of fibers is defined by the network generation algorithm and has a Poisson distribution characterized by the mean fiber length, l_c. Parameter L_0 used in the context of non-crosslinked networks is replaced in this case by l_c, which becomes the only characteristic length associated with the network structure.

The mean connectivity number, $\bar{z}$, i.e. the number of fibers emerging from a node, is $\bar{z} = 6$ and $\bar{z} = 3.5$ in the Delaunay and Voronoi cases considered, respectively. Note that the Voronoi procedure leads to 2D networks with $\bar{z} = 3$. We increase $\bar{z}$ in the present case by merging the nodes that bound the shortest segments. This procedure is applied until $\bar{z} = 3.5$, which corresponds to collagen biopolymer networks (Lindström et al., 2010). The nodes are considered as pin-joints, and hence transmit forces, but do not transmit moments between fibers. This facilitates the relative rotation of neighboring fibers to enable adhesive interactions.

Pin-jointed structures in 2D with $\bar{z} < 4$ are sub-isostatic (Maxwell, 1864) and their stiffness vanishes under infinitesimal perturbations. Hence, we consider both isostatic (Delaunay) and sub-isostatic (Voronoi) networks. In addition, a diluted Delaunay network (DDN) with $\bar{z} = 4$ is studied for specific system parameters. This network is obtained from a Delaunay network by eliminating fibers. We eliminate fibers for which the sum of the value of z at the two end nodes is significantly larger than 8, such to minimize the variance of z in the resulting network.

It is also important to note that pin-jointed networks without adhesion are actually networks of trusses, since moments are not transmitted at cross-links between fibers, and bending is not engaged. In the presence of adhesion, the bending deformation mode is activated by the adhesive interactions and plays an essential role in mechanics (Section 3).

Given that adhesive interactions are short range, adhesion has to be enabled by an external agent. This 'activation' can be produced mechanically, by capillary forces or by other means. Specifically, consider the detail of the Delaunay network in Fig. 1(a) shown in Fig. 2. The fibers of the network in Fig. 2(a) do not interact adhesively in the initial configuration since they are too far apart. To enable such interactions, we use a proximity criterion. Specifically, we select pairs of neighboring fibers and allow them to rotate at node O such to align their tangents. Neighboring fibers are paired if the angle separating them is smaller than a specified threshold θ_{th} ($\theta_{th} = 45^0$ for DN and $\theta_{th} = 180^0$ for VN and DDN). In the DN case, modifying the threshold to 70^0 or larger does not lead to different structures after relaxation since de-bundling takes place. The threshold of $\theta_{th} = 180^0$ used for VN and DDN means that all fibers merging into a node are initially bundled. Debundling takes place during structural relaxation as dictated by the balance of strain and adhesion energies (Section 2.2). Stochastic

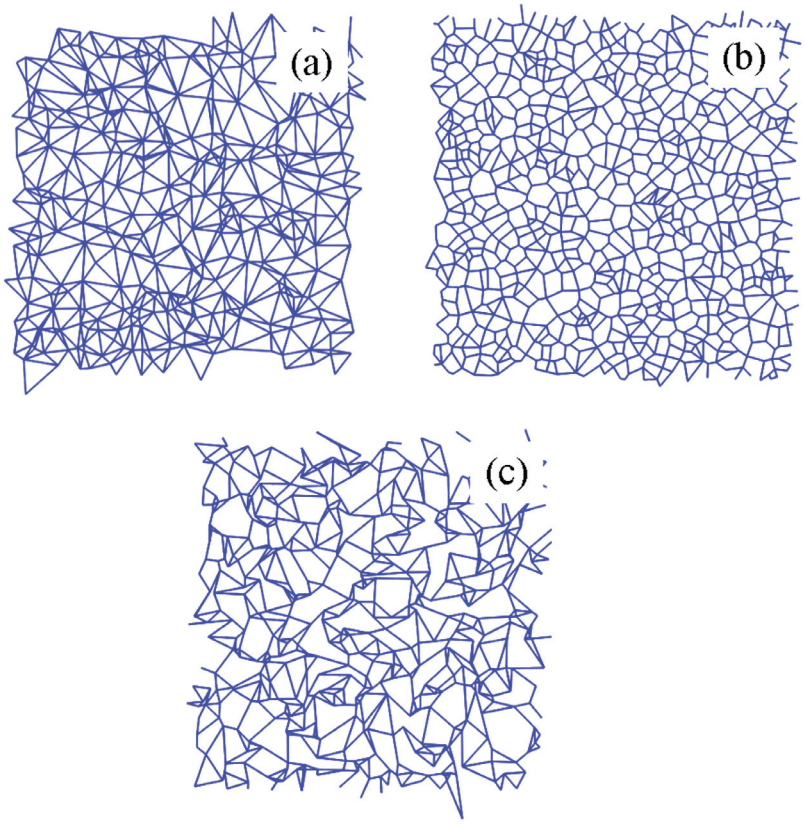

Fig. 1. Examples of 2D (a) Delaunay, (b) Voronoi and (c) diluted Delaunay networks considered in this study.

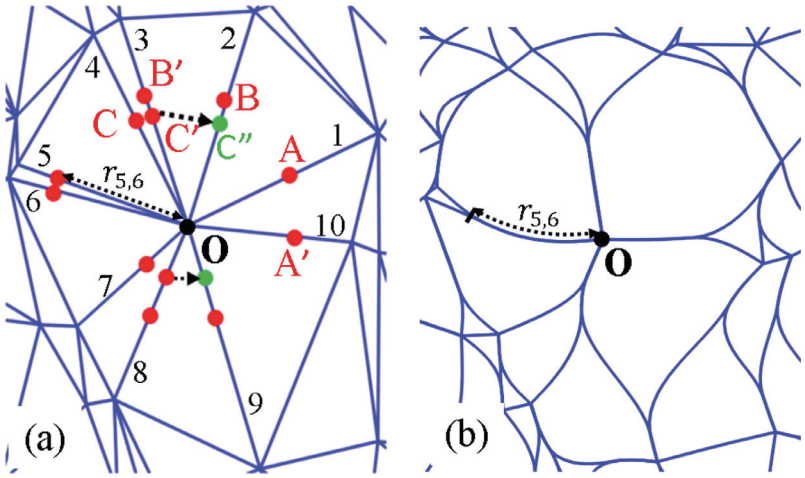

Fig. 2. Detail of a Delaunay network showing (a) the initial state before activation and (b) the stable, relaxed configuration resulting from the activated state resulting from (a).

bundling, i.e. bundling of fibers which are not immediately adjacent, could in principle take place in 3D, but such structures are expected to have higher strain energy and hence should not be favored relative to those bundled based on fiber proximity.

Since the network may bundle in numerous ways and multiple locally stable states exist in the phase space of all possible bundled topologies, the phase space was sampled by devising a geometric parametrization scheme which uniquely defines a specific bundled topology. Further, an energy minimization procedure was employed to search for a local energy minimum

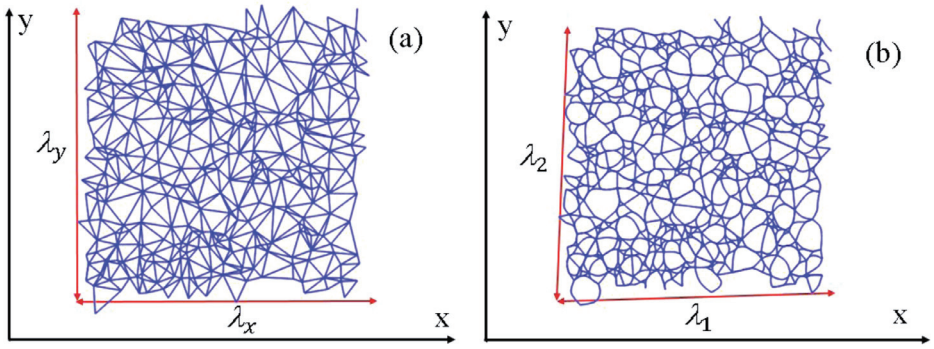

Fig. 3. (a) Initial and (b) relaxed states of a DN network.

in this topological phase space. The relaxed configuration resulting from the activated state of the initial configuration in Fig. 2(a) is shown in Fig. 2(b).

The physical quantities used to describe this problem are E_fI, E_fA, l_c, and γ. The Buckingham-π dimensional analysis indicates that two non-dimensional groups can be produced using these quantities. These may be written as $\Psi = (l_c/L_{EC})^2 = \gamma l_c^2/E_fI$ and $\phi = l_c^2E_fA/E_fI$, which have physical meaning. Ψ indicates the strength of adhesion and ϕ is the square of the mean slenderness-ratio of the fibers (considering fibers of circular section, $l_b^2 = E_fI/E_fA \sim d^2$, with d being the fiber diameter). Parameter Ψ is central to the present discussion. We consider networks of large ϕ (in the range 2.5×10^3 to 10^4) such to allow adhesion to effectively produce fiber bundling. Bundling becomes less effective as ϕ decreases and the network mechanics reverts to that of usual cross-linked networks without adhesion. Note that the high slenderness ratio case is also relevant for most biological networks of nanofibers.

In the following, we refer to four states of the network: (1) 'initial,' which represents the geometry produced by the Delaunay or Voronoi procedures, (2) 'activated,' which represents the initial state of bundling, (3) 'relaxed,' representing the stable structure of bundled fibers obtained by energy minimization from the 'activated' state, and (4) 'loaded,' representing any of the network states subjected to an imposed deformation. Fig. 3(a) shows an example of DN in the initial state, while Fig. 3(b) shows the corresponding relaxed state.

2.2. Solution method

The parametrization used to define bundling is shown in Fig. 2. For a generic fiber i, parameter r_{ij} defines the length of bundling with fiber j. This length is measured along the curvilinear contour of the fiber (Fig. 2(b)). The problem considered in this work is defined in the space of the set of parameters $\{r_{ij}\}$ and a set of vector-valued displacement functions $\{\breve{\mathbf{w}}_k\}$, one for each fiber in the network. The deformed position of the kth fiber is $\breve{\mathbf{x}}_k(s) = \breve{\mathbf{X}}_k(s) + \breve{\mathbf{w}}_k(s)$, where $\breve{\mathbf{X}}_k$ is the undeformed position and s is the contour-length parameter. The topology of the network is entirely defined by $\{r_{ij}\}$ and $\{\breve{\mathbf{w}}_k\}$.

The total strain energy of the system U_s is a functional of the set of displacement functions, $\breve{U}_s(\{\breve{\mathbf{w}}_k\})$. The total adhesion energy U_γ is a function of parameters $\{r_{ij}\}$, $\breve{U}_\gamma(\{r_{ij}\})$. A feasible set of displacement functions $\{\breve{\mathbf{w}}_k\}$ must satisfy the kinematic constraints imposed by parameters $\{r_{ij}\}$. These bundling constraints are of equality type and can be symbolically expressed as $\breve{\mathbf{C}}(\{\breve{\mathbf{w}}_k\}, \{r_{ij}\}) = 0$. The periodic stress-free and fixed/Dirichlet boundary conditions of a periodic network can be described by introducing additional solution variables $\{a_k\}$ (traction-free) and/or pre-specified parameter set $\{b_k\}$ (Dirichlet boundary condition), as described in Section 2.3. These boundary conditions also place equality-type constraints on the system and hence can be generically expressed as $\breve{\mathbf{B}}(\{\breve{\mathbf{w}}_k\}, \{a_k\}, \{b_k\}) = 0$.

The solution to the problem can be obtained by minimizing the total energy, with $\{b_k\}$ specified, as shown in Eq. (1). Note that while $\{r_{ij}\}$ and $\{a_k\}$ form a real-valued vector space, $\{\breve{\mathbf{w}}_k\}$ forms a vector space of functions.

$$\begin{aligned} &\min_{\{\breve{\mathbf{w}}_k\},\ \{r_{ij}\},\ \{a_k\}} \breve{U}_s\left(\left\{\breve{\mathbf{w}}_k\right\}\right) - \breve{U}_\gamma\left(\left\{r_{ij}\right\}\right) \\ &s.t. \quad \breve{C}\left(\left\{\breve{\mathbf{w}}_k\right\}, \left\{r_{ij}\right\}\right) = \mathbf{0}\ ;\ \breve{\mathbf{B}}\left(\left\{\breve{\mathbf{w}}_k\right\}, \left\{a_k\right\}, \left\{b_k\right\}\right) = \mathbf{0} \end{aligned} \tag{1}$$

This minimization problem can be decomposed into a sequential two-level minimization procedure outlined by Eq. (2). The two steps of the solution are defined over different spaces. The minimization expressed by Eq. (2a) is denoted as the 'main problem,' while Eq. (2b) represents the 'sub-problem.'

$$\min_{\{r_{ij}\}} \breve{U}_s\left(\left\{\breve{\mathbf{w}}^*{}_k(r_{ij})\right\}\right) - \breve{U}_\gamma\left(\left\{r_{ij}\right\}\right) \tag{2a}$$

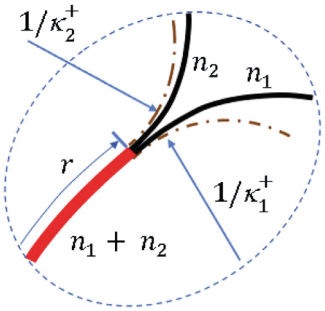

Fig. 4. Representation of a bundle branching for given. $\{\breve{\mathbf{w}}_k^*\}$. r defines the position of the branching point, n_1 and n_2 are bundle sizes, and κ^+ are the curvatures at the branching point of the smaller bundles.

$$\min_{\{\breve{\mathbf{w}}_k\},\ \{a_k\}} \breve{U}_s\left(\left\{\breve{\mathbf{w}}_k\right\}\right) \quad s.t. \quad \breve{C}\left(\left\{\breve{\mathbf{w}}_k\right\},\{r_{ij}\}\right)=\mathbf{0}\ ;\breve{\mathbf{B}}\left(\left\{\breve{\mathbf{w}}_k\right\},\{a_k\},\{b_k\}\right)=\mathbf{0} \tag{2b}$$

$\{\breve{\mathbf{w}}^*{}_k\}$ in Eq. (2a) represents the solution to the minimization sub-problem of Eq. (2b), with $\{r_{ij}\}$ and $\{b_k\}$ as inputs.

The solution method is based on the first order Karush–Kuhn–Tucker (KKT) stability conditions for the main problem of Eq. (2a). The stability conditions require $\partial\breve{U}_s(\{\breve{\mathbf{w}}^*{}_k(r_{ij})\})/\partial r_{lm}$ and $\partial\breve{U}_\gamma(\{r_{ij}\})/\partial r_{lm}$ for a given bundled topology, $\{\breve{\mathbf{w}}^*{}_k\}$, to be obtained from solving the sub-problem of Eq. (2b).

Semi-analytic expressions are derived for $\partial\breve{U}_s(\{\breve{\mathbf{w}}^*{}_k(r_{ij})\})/\partial r_{lm}$ and $\partial\breve{U}_\gamma(\{r_{ij}\})/\partial r_{lm}$. Consider a branched bundle, as shown in Fig. 4. The branching point is defined by a contour parameter r (we drop the two subscripts since r refers to a generic bundle length, i.e. it can be any term of the set $\{r_{ij}\}$). At the branching point a parent bundle having (n_1+n_2) constituent fibers splits into bundles of sizes n_1 and n_2 fibers. These bundles are cotangent and coincident at the branching point. The number of contacts between the constituent fibers in a bundle of size n is denoted by a function $P(n)$. $P(n)$ is determined assuming that the maximum possible number of line contacts are formed, i.e. the bundle is close packed. In this case, $P(n)=3n-\sqrt{12n-3}$ (Harborth, 1974). The partial derivative of the adhesive energy, $\partial\breve{U}_\gamma(\{r_{ij}\})/\partial r$, can be written:

$$\partial\breve{U}_\gamma\left(\left\{r_{ij}\right\}\right)/\partial r=\gamma P(n_1)+\gamma P(n_2)-\gamma P(n_1+n_2) \tag{3}$$

The partial derivative of the total strain energy $\partial\breve{U}_s(\{\breve{\mathbf{w}}^*{}_k(r_{ij})\})/\partial r$ is derived assuming that fibers are inextensible. Eq. (4) shows the expression of this derivative in terms of the bundle sizes and curvatures, κ_1^+ and κ_2^+ (the derivation of Eq. (4) is provided in the Appendix). This expression applies to each branching point in the network provided there are no body forces, and the boundary conditions, $\breve{\mathbf{B}}(\{\breve{\mathbf{w}}_k\},\{a_k\},\{b_k\})$, are either fixed and/or traction-free, i.e. no work is done by external forces.

$$\frac{\partial\breve{U}_s\left(\left\{\breve{\mathbf{w}}^*{}_k(r_{ij})\right\}\right)}{\partial r}=\frac{1}{2}\frac{n_1n_2}{n_1+n_2}EI\left\|\kappa_1^+-\kappa_2^+\right\|^2 \tag{4}$$

$\partial\breve{U}_s(\{\breve{\mathbf{w}}^*{}_k(r_{ij})\})/\partial r$ determines the driving force for bundle unzipping which leads to a decrease of r. On the other hand, $\breve{U}_\gamma(\{r_{ij}\})/\partial r$, which is equal to the work of separation per unit length of the bundle at the branching point, determines the driving force for zipping and increase of r. The stability of a bundle branching is, therefore, determined by the equilibrium between these two opposing forces as per the first-order necessary KKT conditions. Note that the second-order sufficiency KKT conditions cannot be evaluated since $\partial^2\breve{U}_s(\{\breve{\mathbf{w}}^*{}_k(r_{ij})\})/\partial r\partial r'$, where r and r' are two $\{r_{ij}\}$ parameters in the system, cannot be computed analytically.

The sub-problem (Eq. 2(b)) is a variational problem, as it is defined over a vector space of functions $\{\breve{\mathbf{w}}_k\}$, with constraints. This becomes a purely beam mechanics problem with constraint forces and moments required to satisfy the bundling and boundary conditions for the respective beam. The first-order necessary stability conditions of this problem are, therefore, just the governing equations of beam mechanics. The method used to obtain the solution of the sub-problem and main problem is described in Section 2.3.

Two stages of the network evolution are discussed: a relaxation stage, in which the network evolves from the activated state to the corresponding relaxed state of minimum energy under traction-free boundary conditions, and a loading stage, in which the network deforms starting from the relaxed state, under prescribed displacement or mixed boundary condition.

2.3. Implementation

The numerical solution of the sub-problem requires discretization of the vector space of the displacement functions $\{\breve{\mathbf{w}}_k\}$. A finite element (FEM) procedure is employed for this purpose. The fibers are represented with 2 node linear Timoshenko beam elements. The bundling of two fibers and the co-location and co-tangency at the point of their separation are represented through linear kinematic constraint equations. This requires placing mesh nodes at bundle branching points and these nodes must be mobile for the discretization to adapt to the evolving bundles during loading and relaxation, i.e. the discretization for the sub-problem depends on $\{r_{ij}\}$.

The mesh nodes are classified into four categories denoted as order zero to order three. The 'zero-order' nodes are those representing the cross-links of the network. The 'order one' nodes are created directly from the lengths $\{r_{ij}\}$ of the bundling fibers and define the point of separation of the respective fiber pair, e.g. points A and A′ and B and B′ in Fig. 2(a). However, at any such branching point, force and moment redistribution takes place between all fibers in the participating bundle. Hence, it becomes necessary to introduce 'order two' nodes on all fibers in the respective bundle, co-located with the 'order one' node of each sub-bundle that branches out. In Fig. 2(a), nodes C and C′ are of 'order one,' while node C″, which is a 'order two' node, is introduced on fiber O2 at the location of the separation of fibers O3 and O4, co-located with C and C′. The 'order two' nodes are created based on the 'order one' nodes using a Depth-First Tree Traversal method of a node projection operation (Even, 1979). The 'order three' nodes are used for mesh refinement and are introduced between the 'order one' and/or 'order two' nodes on each fiber such that there are at least 30 elements per each segment of length l_c.

Periodic boundary conditions are applied to the network in both in-plane directions. These are defined by the periodic lengths λ_x and λ_y (Fig. 3). In the initial state of the network, before relaxation, $\lambda_x = \lambda_y = L$. Relaxation under the action of adhesive forces introduces eigenstrains and the simulation cell distorts, such that the directions of periodicity may not remain orthogonal (Fig. 3(b)).

The applied deformation is defined by the global deformation gradient

$$\mathbf{F} = \begin{bmatrix} 1+\xi_{11} & \xi_{12} \\ \xi_{12} & 1+\xi_{22} \end{bmatrix} \tag{5}$$

in terms of which the periodic boundary conditions can be written as: $\mathbf{x}^* = \mathbf{x} + \mathbf{F}\cdot(\mathbf{X}^* - \mathbf{X})$, where $\mathbf{x}^*$, $\mathbf{x}$ are the deformed position of any two corresponding points on the periodic boundaries and $\mathbf{X}^*$, $\mathbf{X}$ are the respective undeformed positions. Parameters ξ_{11}, ξ_{12}, ξ_{22} are not specified for the relaxation simulation, $\{a_k\} = \{\xi_{ij}\}$ and $\{b_k\} = \emptyset$, such that the structure evolves from the activated state under traction free boundary conditions. The global deformation gradient obtained for the relaxed state at the end of the evolution is denoted by $\mathbf{F^R}$. The imposed deformation is performed under mixed boundary conditions and represents uniaxial tension. Specifically, an applied deformation gradient, $\mathbf{F^d}$, is defined with respect to the relaxed state in which parameter ξ^d_{22} is specified, while $\{\xi^d_{11}, \xi^d_{12}\}$ are set free, i.e. $\{a_k\} = \{\xi^d_{11}, \xi^d_{12}\}$ and $\{b_k\} = \{\xi^d_{22}\}$. Thus, the global deformation gradient with respect to the initial state is $\mathbf{F} = \mathbf{F^d}\cdot\mathbf{F^R}$.

The FEM analysis is performed quasi-statically using the explicit time integration scheme in the commercial finite element software ABAQUS, version 6.11. The analysis requires an iteration that has two steps: solution mapping and incremental loading. In the solution mapping step, the nodal solution of the sub-problem from the previous iteration of the main-problem is mapped onto the current mesh nodes using spline interpolation. This helps maintain the continuity of the evolution trajectory and also reduces the simulation time. In the incremental loading step, the linear kinematic constraint equations and the boundary conditions corresponding to $\{r_{ij}\}$ and $\{b_k\}$ for the current iteration of the main-problem are applied.

To solve the main problem, we use a gradient descent algorithm. The gradients of $\breve{U}_s(\{\breve{\mathbf{w}}^*_k(r_{ij})\})$ and $\breve{U}_\gamma(\{r_{ij}\})$ in the $\{r_{ij}\}$ space are available once the sub-problem is solved for a given $\{r_{ij}\}$. However, the solution state variables $\{r_{ij}\}$ are bounded $\{r_{ij}|\ r_{ij} \geq 0\ \&\ r_{ij} \leq \min(l_i,\ l_j)\}$, where l_i and l_j are the lengths of the fibers associated with parameter r_{ij}. This implies that the first order optimality conditions are modified as $\partial\breve{U}_s(\{\breve{\mathbf{w}}^*_k(r_{ij})\})/\partial r_{lm} - \partial\breve{U}_\gamma(\{r_{ij}\})/\partial r_{lm} = 0$ only if $r_{lm} > 0$ & $r_{lm} < \min(l_l,\ l_m)$ and $\partial\breve{U}_s(\{\breve{\mathbf{w}}^*_k(r_{ij})\})/\partial r_{lm} - \partial\breve{U}_\gamma(\{r_{ij}\})/\partial r_{lm} \leq 0$ if $r_{lm} = \min(l_l,\ l_m)$ and ≥ 0 if $r_{lm} = 0$. However, the case of $r_{lm} = 0$ is not physically possible since unstable fiber bundles of 0 sticking lengths cannot exist. Therefore, if a certain r_{lm} reaches zero during the evolution, and $\partial\breve{U}_s(\{\breve{\mathbf{w}}^*_k(r_{ij})\})/\partial r_{lm}$ - $\partial\breve{U}_\gamma(\{r_{ij}\})/\partial r_{lm} > 0$, the particular parameter, r_{lm}, is removed from the parameters list $\{r_{ij}\}$ and the co-tangency condition between the lth and the mth fibers is eliminated. This modifies the main problem allowing for de-bundling of fiber pairs, which implies that the dimensionality of the parameter space $\{r_{ij}\}$ decreases. The gradient descent optimization is performed with a small but adaptive step-size. We verify that the resulting state is independent of the step-size. The stopping criterion of the minimization requires that the total energy variation over 5 iterations is smaller than 0.5%.

3. Results

The structure and the response to uniaxial tension and compression of DN, VN and DDN are discussed in this section. Adhesion is defined in terms of the non-dimensional parameter $\Psi = (l_c/L_{EC})^2$ which takes values between 0.3 and 11 for the DN case, and between 0.3 and 3 for the VN case. The connection with specific network systems has to be established

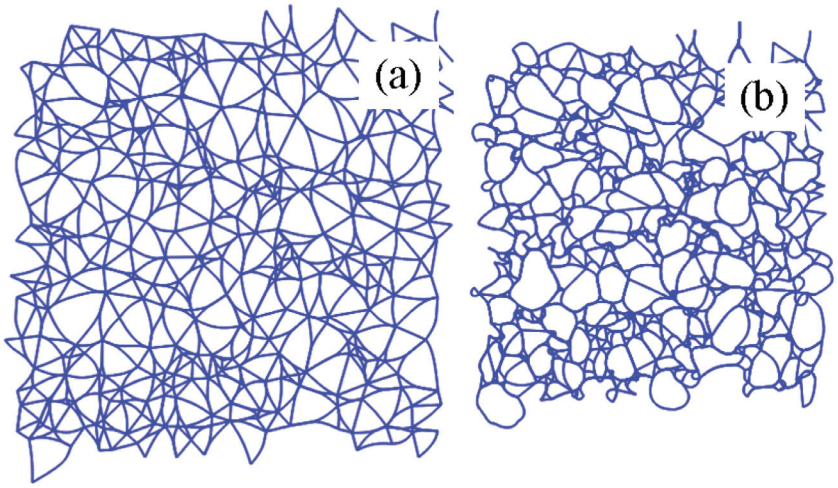

Fig. 5. Relaxed state network configurations for DN with (a) $\Psi = 1$ (b) $\Psi = 11$.

via L_{EC}, which is a material property. The ranges of Ψ considered correspond to networks with mean segment length l_c in the range $0.5L_{EC}$ – $3.3L_{EC}$ in the DN case, and to $l_c \in (0.5L_{EC}$ – $1.7L_{EC})$ in the VN case. Thus, for the case of actin networks, l_c is in the range 0.23 μm – 0.8 μm which would correspond to (unbundled) 3D networks of density in the range 0.26 mg/ml – 3 mg/ml. Likewise, for the microtubules case, l_c covered in this study is in the range 6.75 μm – 22.95 μm, which corresponds to unbundled 3D networks of densities 0.3×10^{-2} mg/ml to 3.6×10^{-2} mg/ml. The conversion from 2D to 3D densities was made assuming 3D Voronoi networks of same l_c as the 2D model, and a linear mass for F-actin of 16,000 Da/nm and for microtubules of 160,000 Da/nm.

The DDN is used to study the effect of mean connectivity, $\bar{z}$, for $\Psi = 2$. Three realizations are considered for each Ψ and for each type of network, and the results reported represent the average of the response of these realizations.

3.1. The structure of cross-linked networks with adhesion

Under zero traction boundary conditions, adhesion leads to a Ψ-dependent reduction of the total area of the structure. In this process, the (absolute value) adhesion energy and the strain energy increase. Evolution stops when the incremental increase of the strain energy becomes larger than the corresponding increase of the adhesion energy.

Fig. 5 shows the relaxed state of Delaunay networks with $\Psi = 1$ (Fig. 5(a)) and $\Psi = 11$ (Fig. 5(b)). The variation with Ψ of the absolute value of the dilatation strain $\delta = 1 - J = 1 - A_0/A$ (where J is the Jacobian of the transformation and A_0, A are the model areas in the initial and relaxed states, respectively) during relaxation is shown in Fig. 6(a). In the low adhesion regime, $\Psi < 1$, the number of bundles varies rapidly with Ψ, while the individual bundle size is approximately constant. For larger Ψ values, the number of bundles is approximately independent of Ψ, while the bundle size increases. This second regime is characterized by a power law dependence of δ on Ψ, with exponent 1.22.

The variation of the strain, U_s, and adhesion, U_γ, energies of the relaxed DN state with Ψ is shown in Fig. 6(b). To facilitate the interpretation, the two energies are written as:

$$U_s = \left(\frac{N_f E_f I}{l_c}\right)\left(\frac{\overline{\kappa^2} l_c^2}{2}\right) = \left(\frac{N_f E_f I}{l_c}\right)\hat{U}_s \tag{6a}$$

$$U_\gamma = \left(N_f l_c \gamma\right)\overline{\left(\frac{P(n)}{n}\right)} = \left(N_f l_c \gamma\right)\hat{U}_\gamma \tag{6b}$$

Here N_f represents the number of fibers in the structure and the groups $\frac{N_f E_f I}{l_c}$ and $N_f l_c \gamma$ do not vary during relaxation or deformation. The non-dimensional energies $\hat{U}_s$ and $\hat{U}_\gamma$ are shown in Fig. 6(b). These quantities vanish in the initial state. The curves exhibit a dependence on Ψ qualitatively similar to that of δ. For $\Psi > 1$ the dependence of $\hat{U}_s$ and $\hat{U}_\gamma$ on Ψ can be described by power laws of exponents, 1.35 and 0.57, respectively. A more rapid variation is observed for $\Psi < 1$.

Fig. 6(c) shows the data in Figs. 6(a) and (b), with the two energy components being plotted versus the dilatation strain, δ, for the entire range of variation of Ψ. Two power laws emerge, $\hat{U}_s \sim \delta$ and $\hat{U}_\gamma \sim \delta^{1/2}$, which are well defined over three orders of magnitude range of δ. The linear scaling of $\hat{U}_s \sim \overline{\kappa^2}$ with δ is expected since the structure undergoes large deformations as it collapses under the action of adhesive forces. The situation is equivalent to the post-buckling regime of a beam. The variation of $\hat{U}_\gamma$ as the square root of the dilatation strain represents the re-organization of the structure under the action of adhesive forces and cannot be explained based on simple considerations.

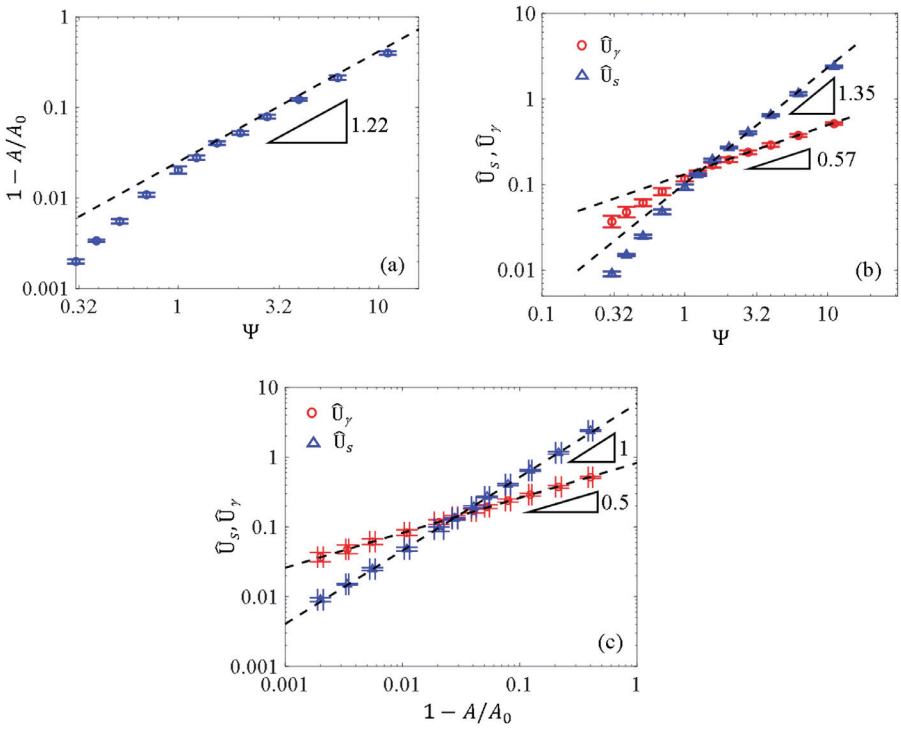

Fig. 6. Variation of (a) the reduction of area and (b) the normalized strain and adhesion energies of DN between the initial and relaxed states as function of Ψ. The reduction of area is shown versus the normalized energies in (c). The bars represent the standard error for three replicas for each system.

The VN exhibits quite different behavior. This type of network is sub-isostatic in the initial state and adhesive forces produce dramatic structural collapse. The network area decreases by over 80% between the initial and relaxed states, even for rather small values of Ψ. The dependence of the total shrinkage on Ψ is weak for any Ψ, Fig. 7(a). The area reduction is finite for finite Ψ, unlike the DN case in which $\delta \to 0$ as $\Psi \to 0$. Fig. 7(b) shows the variation of the normalized energies of Eq. (6) with Ψ. These are power functions for the entire range of variation considered for Ψ, $\hat{U}_s \sim \Psi^{1.35}$ and $\hat{U}_\gamma \sim \Psi^{0.37}$. The exponents are close to those obtained for DN (Fig. 6) since the same physics controls the structural collapse.

The DDN network with $\bar{z} = 4$ is at the isostatic critical point. The network with $\Psi = 2$ develops a large dilatation strain δ of approximately 40%, which is between the corresponding values obtained for the same Ψ for DN and VN, i.e. $\delta = 5\%$ and $\delta = 88\%$, respectively. Since adhesion stabilizes sub-isostatic networks, the state characterized by $\bar{z} = 4$ is not a critical point for these structures.

From a practical point of view, this result indicates that in the presence of adhesion networks are always mechanically stable. Adhesion-stabilized configurations are states of the network qualitatively different from cross-linked networks without adhesion and which exhibit specific mechanical behavior, as discussed in the next section.

It is also of interest to discuss the dependence of the degree of bundling on Ψ. Fig. 8 shows the variation of the mean number of fibers in a bundle, $\bar{s}_b$, with Ψ for DN and VN in the relaxed state. Un-bundled single fibers are not considered in this averaging. $\bar{s}_b$ is normalized by the average connectivity number, $\bar{z}$, in the respective structure. In the DN case, with $\bar{z} = 6$, the limit as Ψ tends to 0 is 2/6 since at least two fibers are required to form a bundle. The degree of bundling increases continuously with Ψ, as expected. A similar trend is observed for the VN relaxed states. For the VN, the normalization is done with $\bar{z} = 3.5$. It is insightful to note that the $\bar{s}_b$ for VN is higher than for DN at any given Ψ even though the DN has a higher mean coordination number than VN. For example, at $\Psi = 3$ the DN has $\bar{s}_b = 2.22$ whereas VN has $\bar{s}_b = 2.73$. This highlights a significantly higher level of bundling in the VN compared to DN owing to their floppy nature.

3.2. Response in tension

Relaxed DN and VN structures are deformed in uniaxial tension and compression by controlling parameter ξ^d_{22} of Eq. (5). A non-zero stress Π_{22} develops, while the other stress components vanish. We use the second Piola–Kirchhoff stress, $\mathbf{\Pi}$, and the Green–Lagrange strain, $\mathbf{E}$, as work conjugate stress and strain measures. $\mathbf{\Pi}$ is computed from the nominal stress, $\mathbf{S}$, as $\mathbf{\Pi} = \mathbf{F}^{-1}\mathbf{S}$. The stress, $\mathbf{\Pi}$, and the tangent stiffness, K_t, are normalized by $E_f I/l_c^3$, where l_c is measured in the initial state. The normalized stress and elastic modulus are denoted by $\hat{\mathbf{\Pi}}$ and $\hat{K}_t$, respectively.

DN without adhesion ($\Psi = 0$) subjected to uniaxial tension exhibits three regimes. Fig. 9(a) shows the stress-strain response, $\hat{\Pi}_{22}(\hat{E}_{22})$, while Fig. 9(b) shows the tangent stiffness vs. stress plot, $K_t = d\hat{\Pi}_{22}/d\hat{E}_{22}$ vs. $\hat{\Pi}_{22}$ (black dashed line). At

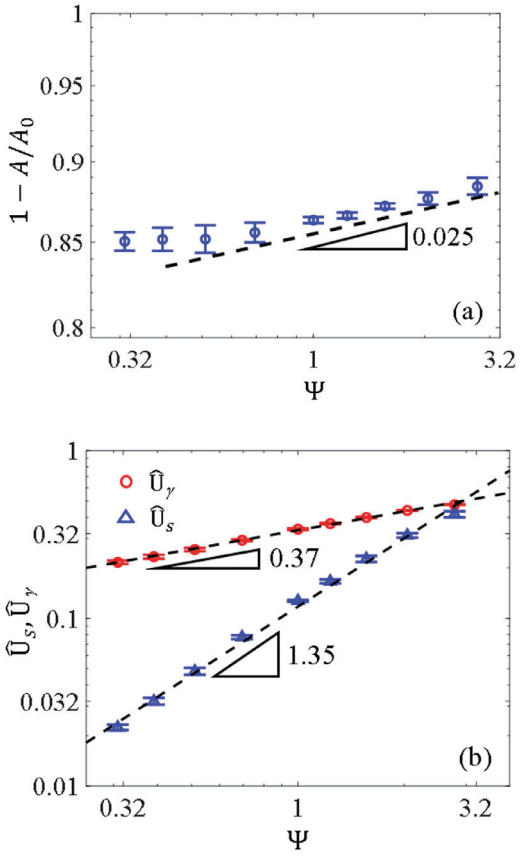

Fig. 7. Variation of (a) the reduction of area and (b) the normalized strain and adhesion energies of VN between the initial and relaxed states as function of Ψ. The bars represent the standard error for three replicas for each system.

small strains, the structure stores energy predominantly in the axial deformation mode of fibers. Fibers aligned with the loading direction are predominantly subjected to tension, while those oriented approximately orthogonal to the loading direction are predominantly in compression. A distinct loss of stability event is observed when the transverse fibers buckle in compression, leading to a decrease of the tangent stiffness. This enables the fibers to re-orient in the direction of the tensile loading, which leads to the formation of stress paths (Žagar et al., 2015).

These features are inherited by the DN with adhesion ($\Psi \neq 0$). However, increasing Ψ causes a rapid decrease of the normalized small strain modulus, $\hat{K}_0$, and the elastic instability observed in the $\Psi = 0$ case becomes less pronounced and is eventually eliminated for large enough values of Ψ. The $\hat{K}_t$ vs. $\hat{\Pi}_{22}$ curves corresponding to different Ψ merge in the third regime, which indicates that in these conditions the influence of adhesion is lost, Fig. 9(b).

The side panels of Fig. 9(a) show deformed configurations of a network with $\Psi = 1.23$ at 5% strain and a network with $\Psi = 11.11$ at 25%, respectively. These two states correspond to the same stress level in the range of transition from the adhesion-controlled part of the stress-strain curves to the network-controlled part. In these conditions, the network strain-stiffens, and stress paths begin to form.

Fig. 9(c) shows the variation of the network volume, normalized with the volume of the relaxed state, during deformation. Networks with small Ψ contract strongly due to the large Poisson effect commonly observed in networks without adhesion. As Ψ increases, this contraction is eliminated for the duration of the linear response of the network. Once the system enters the network-dominated strain stiffening regime, volume reduction is observed, similar to the case without adhesion.

The most interesting feature observed in Fig. 9 is the significant increase of the strain range corresponding to the initial linear elastic regime as Ψ increases. Adhesion reduces the effective stiffness and makes the behavior linear over a larger strain range. If no structural rearrangements take place (e.g. by reorganization of bundles), the response is reversible since adhesion brings the structure back to the initial (relaxed) configuration upon unloading.

From a network design perspective, it is apparent that considering inter-fiber adhesion provides new opportunities. The results indicate that the small strain regime of the deformation is controlled by adhesive interactions, while the large strain regime is dominated by the behavior of the cross-linked network. Tuning adhesion allows modifying the initial material stiffness over a broad range and also increases the range of linear behavior up to strains as large as 20%. The strain at

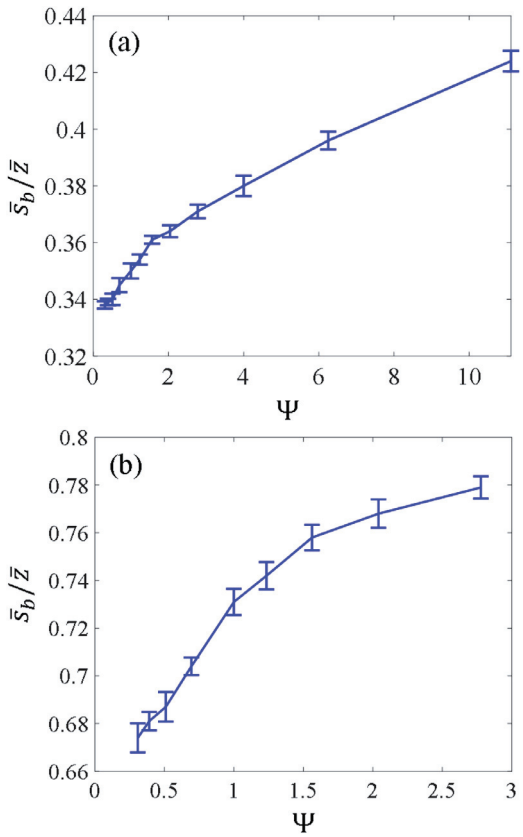

Fig. 8. Variation of normalized mean bundle size $\bar{s}_b$ for (a) the DN relaxed states and (b) the VN relaxed states as a function of Ψ. The bars represent the standard error for three replicas for each system.

which strain stiffening begins is also tunable by changing Ψ. It is likely that these effects are operating in biological fibrous materials.

The variation of the normalized small strain modulus, $\hat{K}_0$, with Ψ is shown in Fig. 10. $\hat{K}_0$ decreases rapidly with increasing Ψ and tends toward an asymptotic value, $\hat{K}^*$, at large Ψ. A well-defined power law represents this variation in the range of Ψ studied. Over two decades of Ψ, $\hat{K}_0 - \hat{K}^* \sim \Psi^{-1.4}$. The value of the asymptote has low practical importance. It results from the current fitting to be $\hat{K}^* = 116.64$.

A different behavior is exhibited by Voronoi networks loaded in uniaxial tension. The reference case considered above, $\Psi = 0$, is not relevant for VN since these structures are sub-isostatic and their effective stiffness vanishes. Fig. 11(a) shows stress-strain curves for VN with various Ψ values. A stiffening trend is observed in this case as Ψ increases. This effect is entirely due to adhesion.

A striking feature of these stress-strain curves is the reduction of the tangent modulus with increasing strain, as observed in Fig. 11(a). Such response was not reported previously for any cross-linked fiber network without adhesion. The effect is shown in the inset of Fig. 11(a) where the tangent stiffness is plotted versus stress. Fig. 11(b) shows the variation of the small strain modulus with Ψ. The stiffness increases with Ψ. This is in sharp contrast to the behavior of networks which are isostatic ($\bar{z} > z_c$) in the initial configuration, whose small strain modulus decreases as a power law of Ψ (Fig. 10).

Fig. 11(c) shows the variation of the VN volume, normalized with the volume of the relaxed state, during deformation. These networks are entirely controlled by adhesion. The domain expands weakly as the network is stretched, a behavior also seen for the large Ψ values in the DN case (Fig. 9(c)). Hence, once again, adhesion modifies the typical response of the network without adhesion, eliminating the large contraction commonly observed during tensile loading.

Networks of pin-jointed fibers with connectivity smaller than z_c are floppy at small strains in the absence of inter-fiber adhesion. Adhesion reorganizes the structure and renders stiffness non-zero at all strains. This provides an opportunity to engineer network mechanical behavior; both the initial stiffness and the gradual reduction of the tangent modulus during deformation can be tuned broadly by changing Ψ.

In view of the apparent discrepancy of the behaviors of DN and VN structures, we turn now to the DDN case. The connectivity index for these structures is exactly $\bar{z} = 4$ and DDN networks without adhesion are at the limit of isostaticity. Adhesion stabilizes these structures which exhibit a non-zero stiffness in the relaxed configuration, similarly to all VN and DN networks discussed above. The stress-strain curve of the DDN with $\Psi = 2$ is shown in Fig. 12. This curve exhibits an

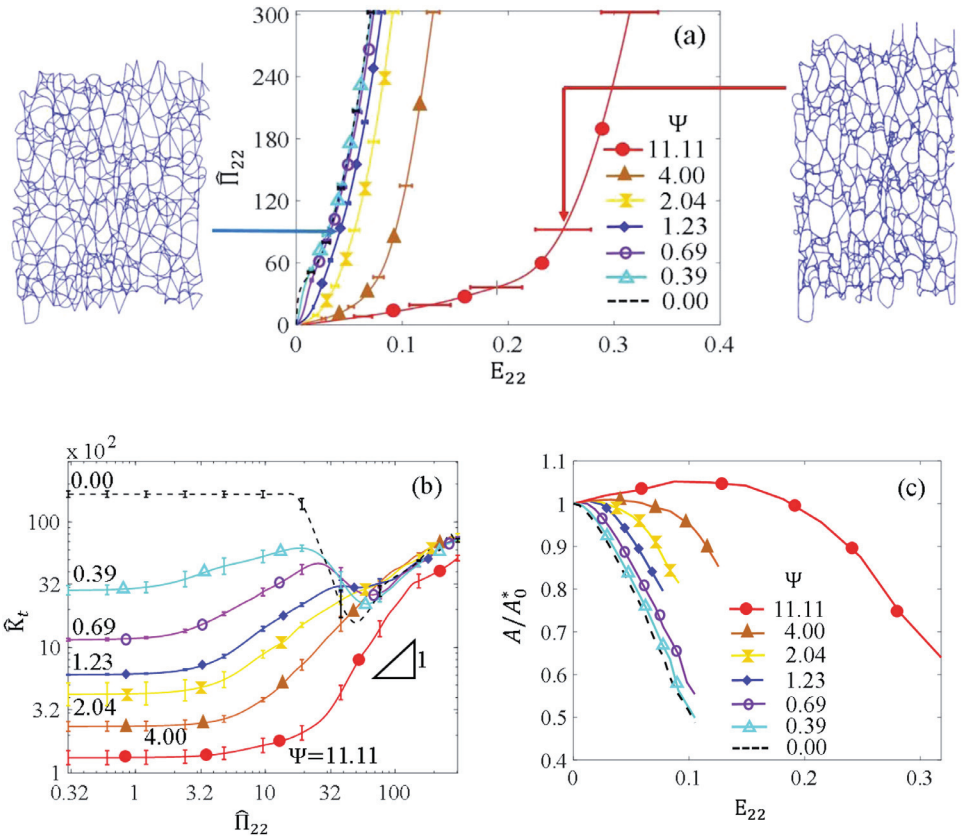

Fig. 9. (a) Normalized second Piola–Kirchhoff stress vs. Green–Lagrange strain for DN with various Ψ subjected to uniaxial tension. The side panels represent deformed configurations with $\Psi = 1.23$ at 5% strain and with $\Psi = 11.11$ at 25% strain. These states correspond to the same stress level. The data in (a) are re-plotted in (b) as normalized tangent stiffness, $\hat{K}_t$, vs. stress. The curve for the system with no adhesion is added for reference (dashed black line). The bars represent the standard error for three replicas for each system. The numbers represent the value of Ψ for each curve. (c) Variation of the network volume (normalized with the volume of the relaxed state A_0^*) during tensile deformation.

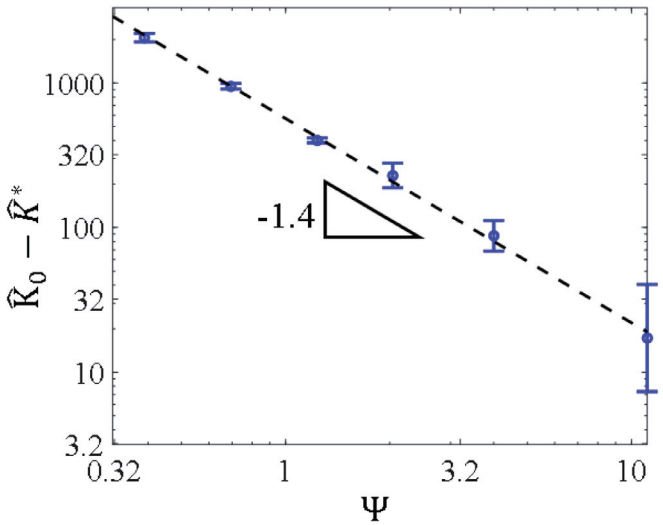

Fig. 10. Variation of the normalized small strain modulus, $\hat{K}_0$, with Ψ for DN. The bars represent the standard error for three replicas for each system.

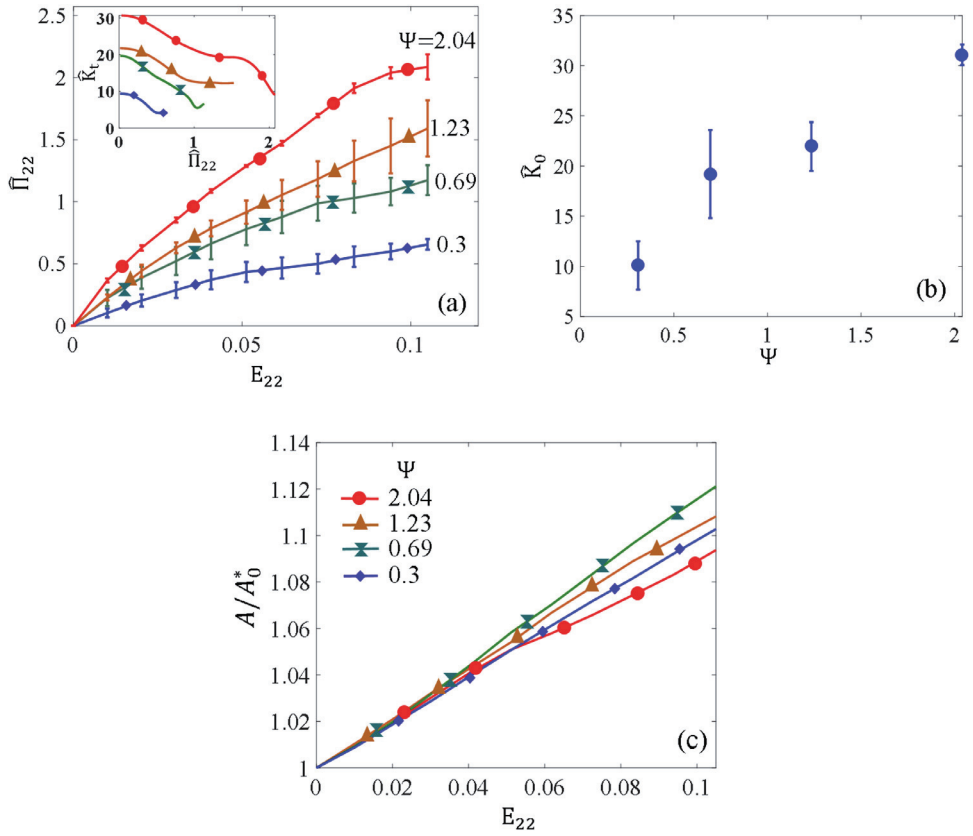

Fig. 11. (a) Normalized second Piola–Kirchhoff stress vs. Green–Lagrange strain for VN with various Ψ subjected to tension. The inset shows the tangent stiffness vs. stress for Ψ values of the main figure. (b) Variation of the normalized small strain modulus with Ψ. The bars represent the standard error for three replicas for each system. (c) Variation of the network volume (normalized with the volume of the relaxed state A_0^*) during tensile deformation.

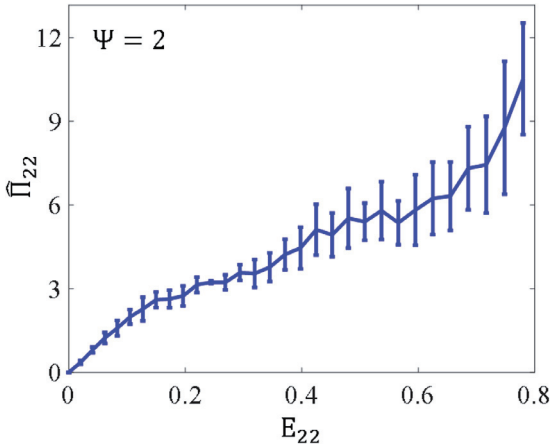

Fig. 12. Normalized second Piola–Kirchhoff stress vs. Green–Lagrange strain for DDN loaded in tension. The bars represent the standard error for three replicas for each system.

initial linear regime, a gradual decrease of tangent modulus with increasing strain, similar to that of the VN networks shown in Fig. 11(a), and a strain-stiffening regime at larger strains, similar to that observed for DN networks, Fig. 9(a). The normalized small strain stiffness $\hat{K}_0$ for the VN ($\bar{z} = 3.5$), DDN ($\bar{z} = 4$) and DN ($\bar{z} = 6$) with the same level of adhesion ($\Psi = 2$) is 31.1, 19.6 and 345.8. The small strain response of DDN is close to that of VN and this reflects in the similarity of the respective $\hat{K}_0$ values. The DN networks are much stiffer.

It is necessary to make a note regarding Mikado-like structures which are models adequate for biological fibrous materials. In such cases, fibers are longer than the distance between two crosslink points and hence each fiber carries multiple

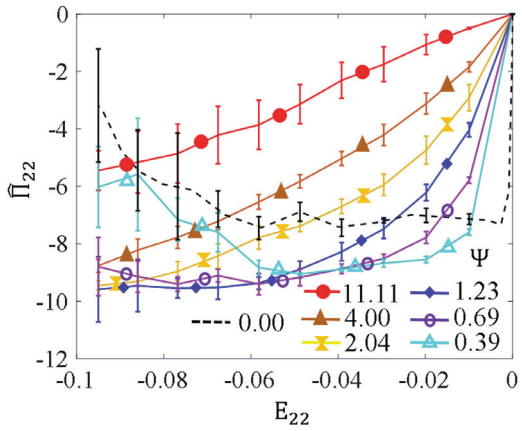

Fig. 13. Normalized second Piola–Kirchhoff stress vs. Green–Lagrange strain for DN networks with various Ψ subjected to uniaxial compression. The bars represent the standard errors for the three realizations.

cross-links. Moments are transmitted along individual fibers, although moments are not transmitted between fibers (if cross-links are represented as pin-joints). This renders the Maxwell estimate of the limit of stability inapplicable to 3D Mikado networks. In such situations, the strain energy penalty associated with the activation of adhesion (i.e. going from the initial to the relaxed configuration) is expected to be larger than that evaluated with the current model. The exact evaluation of this contribution is not trivial and requires a dedicated study. Nevertheless, the physics of the problem being identical (i.e. the competition between the bending strain energy and the adhesion energy), we expect to observe similar phenomenology in Mikado networks, albeit in a different parameter range.

3.3. Response in compression

Fiber networks exhibit in compression a response similar to that of cellular materials. An initial linear elastic regime is followed by strain localization. Strain stiffening is observed at large strains due to the formation of contacts between fibers. Two dimensional models exhibit the first two regimes, while the third regime is not reproduced due to the lack of excluded volume interactions. Fig. 13 shows such behavior for DN networks with $\Psi = 0$. In this case, localization leads to pronounced softening and instability.

The effect of adhesion is shown for DN with $\Psi > 0$ (Fig. 13). Similar to the case of tension, the small strain modulus decreases with increasing Ψ. In fact, the values of K_0 measured in compression for the various curves are identical to those evaluated in tension and reported in Fig. 10. Strain localization and the onset of the second regime is postponed to much larger strains compared with the $\Psi = 0$ case. This effect is identical to that observed in tension – adhesion increases significantly the strain range of the linear response of the network. Furthermore, deformation becomes more stable in the post-localization regime as softening is eliminated.

VN networks undergo large volume reduction during relaxation. Further compression is less physically meaningful than in the DN case. The small strain behavior is similar to that reported in Fig. 13 for the DN networks. Since the structure of VN is already fairly dense due to intense bundling, further compression should lead to rapid strain stiffening commonly observed at large strains in non-adhesive networks and in cellular materials. This cannot be reproduced in 2D due to the lack of excluded volume interactions.

4. Conclusions

Fiber networks in which fibers interact adhesively exhibit a range of mechanical properties not encountered in similar systems without adhesion. Adhesion causes significant volume reduction of the network which becomes stable in a self-equilibrated stressed state. The dilatation strain, stored strain energy and adhesion energy increase approximately as power functions of Ψ. Networks which are sub-isostatic without adhesion ($\bar{z} < z_c$) are stabilized by the adhesive interactions and acquire finite stiffness.

The small strain modulus of the network decreases with increasing the strength of adhesion as a power function of Ψ for isostatic networks ($\bar{z} > z_c$). The opposite effect is observed for sub-isostatic networks ($\bar{z} < z_c$), for which the stiffness increases with increasing Ψ. Interestingly, adhesion extends the small strain linear elastic regime to considerable strains, up to 20%.

The response in tension beyond the linear elastic strain range is also different in the sub-isostatic and isostatic cases. Isostatic networks strain-stiffen at a Ψ–dependent rate. In sub-isostatic networks, the initial linear regime is followed by a gradual decrease of tangent modulus which again increases (strain-stiffens) at larger strains. This apparent decrease of tangent modulus is associated with gradual unbundling and hence is caused by adhesive interactions, while strain-stiffening

at larger strains is associated with preferential fiber orientation, as usually observed in crosslinked networks without adhesion.

In compression, adhesive interactions produce similar effects, reducing the small strain stiffness, extending the strain range of the linear elastic response, and stabilizing the deformation against strain localization at larger strains.

The physics controlling these observations is the interplay between the adhesion and strain energies. Adhesion dominates the behavior at relatively small strains, while the strain energy controls the larger strains response. This observation that emerges from the present 2D models should apply in 3D as well. Softer elastic modes may become available in 3D, which may change the range of parameters in which a specific behavior is observed, but overall the present conclusions are expected to apply to 3D networks as well.

This analysis of the mechanics of cross-linked adhesive fiber networks provides the groundwork for understanding the effects of adhesive interactions in diverse applications ranging from man-made systems of nano-fibers to biological collagen, fibrin and actin networks.

Acknowledgment

This work was supported by the NSF through grant No. CMMI-1634328.

Supplementary materials

Supplementary material associated with this article can be found, in the online version, at doi:10.1016/j.jmps.2018.09.027.

Appendix

The derivation of the partial derivative of the strain energy with respect to the branching point position, $\partial \breve{U}_s(\{\breve{\mathbf{W}}^*\})/\partial r$, is presented here. To simplify notation, we drop the dependence on $\breve{\mathbf{W}}^*$ and refer to the derivative of the total strain energy of the network with respect to a parameter, r, i.e. $\partial U_s/\partial r$. r represents one of the terms in the set $\{r_{ij}\}$, Fig. 4.

The coincidence and co-tangency kinematic constraints for the sub-bundles introduce constraint forces and moments at the bundle ends, which are applied on bundles by the adhesive forces. Consider a generic branching point having a constraint force $\mathbf{F}$ and a constraint moment $\mathbf{M}$ associated with it, and suppose it moves by Δr, as shown in Fig. A1, while all other bundle lengths are kept constant. This can be accomplished by applying forces $\mathbf{F}^*$ and moments $\mathbf{M}^*$ which do work closing the gap between the two sub-bundles at $r+\Delta r$. The total work associated with such evolution is:

$$\Delta \mathrm{W} = \sum_{k=1}^{3} \int_{\Delta x_k}^{0} \mathrm{F}_k^* d\mathrm{u}_k + \sum_{k=1}^{3} \int_{\Delta \theta_k}^{0} \mathrm{M}_k^* d\theta_k \tag{A1}$$

where Δx_k and $\Delta \theta_k$ are the kth components of displacements and rotations required to close the gap between sub-bundles at $r+\Delta r$. All existing constraint forces and moments in the network do not perform work since they act as equal and opposite forces/moments at coincident and co-tangent points. One can reduce notation by observing that in the new configuration $\mathbf{F}^* = \mathbf{F} + \Delta\mathbf{F}$ and $\mathbf{M}^* = \mathbf{M} + \Delta\mathbf{M}$. Using the trapezoidal rule, the two integrals in Eq. (A1) can be written as:

$$\Delta \mathrm{W} = \alpha_F \left(\frac{1}{2} \sum_{k=1}^{3} (\mathrm{F}_k + \Delta \mathrm{F}_k) \Delta \mathrm{x}_k \right) + \alpha_M \left(\frac{1}{2} \sum_{k=1}^{3} (\mathrm{M}_k + \Delta \mathrm{M}_k) \Delta \theta_k \right) \tag{A2}$$

with α_F and α_M being correction factors of order unity.

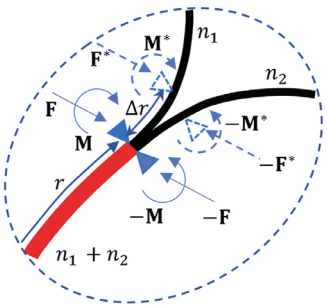

Fig. A1. Forces and moments acting on sub-bundles at two stages of the bundle evolution defined by the extension of the bundle of size $n_1 + n_2$ from length r to length $r+\Delta r$.

Since no external work is performed on the system and no body forces are applied, the variation of the total strain energy is equal to the work done, $\Delta U_s = \Delta W$, and hence:

$$\frac{\partial U_s}{\partial r} = \lim_{\Delta r \to 0} \alpha_F \left(\frac{1}{2} \sum_{k=1}^{3} (F_k + \Delta F_k) \frac{\Delta x_k}{\Delta r} \right) + \alpha_M \left(\frac{1}{2} \sum_{k=1}^{3} (M_k + \Delta M_k) \frac{\Delta \theta_k}{\Delta r} \right) \tag{A3}$$

Retaining only the first order terms,

$$\frac{\partial U_s}{\partial r} = \lim_{\Delta r \to 0} \alpha_F \left(\frac{1}{2} \sum_{k=1}^{3} F_k \frac{\Delta x_k}{\Delta r} \right) + \alpha_M \left(\frac{1}{2} \sum_{k=1}^{3} M_k \frac{\Delta \theta_k}{\Delta r} \right) \tag{A4}$$

which can be concisely rewritten as:

$$\frac{\partial U_s}{\partial r} = \lim_{\Delta r \to 0} \left(\alpha_F \frac{1}{2} |\mathbf{F} \cdot (\boldsymbol{\tau}_2 - \boldsymbol{\tau}_1)| \right) + \left(\lim_{\Delta r \to 0} \alpha_M \right) \frac{1}{2} \left| \mathbf{M} \cdot \left(\kappa_2^+ - \kappa_1^+ \right) \right| \tag{A5}$$

where, $\boldsymbol{\tau}_2$ and $\boldsymbol{\tau}_1$ are the tangent versors of the sub-bundles at the respective branching point and $\boldsymbol{\kappa}_2^+$ and $\boldsymbol{\kappa}_1^+$ are the curvatures of the sub-bundles at the branching point. Due to the co-tangency condition and in the limit $\Delta r \to 0$, $\boldsymbol{\tau}_2 = \boldsymbol{\tau}_1$, and hence Eq. (A5) becomes:

$$\frac{\partial U_S}{\partial r} = \left(\lim_{\Delta r \to 0} \alpha_M \right) \frac{1}{2} \left| \mathbf{M} \cdot \left(\kappa_2^+ - \kappa_1^+ \right) \right| \tag{A6}$$

Even though the system's behavior is non-linear, the incremental deformation can be approximated as linear. Consequently, as $\Delta r \to 0$, α_M tends to 1.

Further, considering the equilibrium of moments at the branching point,

$$\mathbf{M} = \frac{n_1 n_2}{n_1 + n_2} EI \left(\boldsymbol{\kappa}_2^+ - \boldsymbol{\kappa}_1^+ \right) \tag{A7}$$

Therefore, combining Eqs. (A6) and (A7),

$$\frac{\partial U_S}{\partial r} = \frac{1}{2} \frac{n_1 n_2}{n_1 + n_2} EI \left\| \boldsymbol{\kappa}_2^+ - \boldsymbol{\kappa}_1^+ \right\|^2 \tag{A8}$$

Here, we make an assumption that bundles are inextensible, which allows considering that the contour parameter r is identical in the deformed and initial states of the network. Further, due to the short-range nature of adhesion forces, we consider the constraint forces and moments to act at a point, as opposed to being distributed over a segment of the bundles/fibers.

References

Berhan, L., Yi, Y.B., Sastry, A.M., Munoz, E., Selvidge, M., Baughman, R., 2004. Mechanical properties of nanotube sheets: alterations in joint morphology and achievable moduli in manufacturable materials. J. Appl. Phys. 95, 4335–4345. doi:10.1063/1.1687995.

Bico, J., Roman, B., Moulin, L., Boudaoud, A., 2004. Elastocapillary coalescence in wet hair. Nature 432, 690. doi:10.1038/432690a.

Broedersz, C.P., MacKintosh, F.C., 2014. Modeling semiflexible polymer networks. Rev. Mod. Phys. 86, 995–1036. doi:10.1103/RevModPhys.86.995.

Coleman, J.N., Blau, W.J., Dalton, A.B., Muñoz, E., Collins, S., Kim, B.G., Razal, J., Selvidge, M., Vieiro, G., Baughman, R.H., 2003. Improving the mechanical properties of single-walled carbon nanotube sheets by intercalation of polymeric adhesives. Appl. Phys. Lett. 82, 1682–1684. doi:10.1063/1.1559421.

Darnell, M.C., Sun, J.Y., Mehta, M., Johnson, C., Arany, P.R., Suo, Z., Mooney, D.J., 2013. Performance and biocompatibility of extremely tough alginate/polyacrylamide hydrogels. Biomaterials 34, 8042–8048. doi:10.1016/j.biomaterials.2013.06.061.

De Volder, M., Hart, A.J., 2013. Engineering hierarchical nanostructures by elastocapillary self-assembly. Angew. Chem. Int. Ed. doi:10.1002/anie.201205944.

Derjaguin, B.V., Muller, V.M., Toporov, Y.P., 1994. Effect of contact deformations on the adhesion of particles. Prog. Surf. Sci. 45, 131–143. doi:10.1016/0079-6816(94)90044-2.

Erman, B., Mark, J.E., 1997. Structures and Properties of Rubberlike Networks. Oxford University Press.

Even, S., 1979. Graph Algorithms. W. H. Freeman and Co., New York.

Fung, Y.-C., 1993. Biomechanics. Springer, New York. doi:10.1007/978-1-4757-2257-4.

Gibson, L.J., Ashby, M.F., 1999. Cellular Solids: Structure and Properties. Cambridge University Press.

Gittes, F., Mickey, B., Nettleton, J., Howard, J., 1993. Flexural rigidity of microtubules and actin filaments measured from thermal fluctuations in shape. J. Cell Biol. 120, 923–934. doi:10.1083/jcb.120.4.923.

Harborth, H., 1974. Solution to problem 664. Elem. Math. 29, 14.

Head, D.A., Levine, A.J., MacKintosh, F.C., 2003. Distinct regimes of elastic response and deformation modes of cross-linked cytoskeletal and semiflexible polymer networks. Phys. Rev. E 68, 061907. doi:10.1103/PhysRevE.68.061907.

Heussinger, C., Frey, E., 2007. Role of architecture in the elastic response of semiflexible polymer and fiber networks. Phys. Rev. E 75, 011917. doi:10.1103/PhysRevE.75.011917.

Islam, M.R., Picu, R.C., 2018. Effect of network architecture on the mechanical behavior of random fiber networks. J. Appl. Mech. 85, 081011. doi:10.1115/1.4040245.

Israelachvili, J.N., 2011. Intermolecular and Surface Forces, third ed. Academic Press, New York.

Johnson, K.L., 1985. Contact Mechanics. Cambridge University Press, Cambridge. doi:10.1017/CBO9781139171731.

Johnson, K.L., Kendall, K., Roberts, A.D., 1971. Surface energy and the contact of elastic solids. Proc. R. Soc. A Math. Phys. Eng. Sci. 324, 301–313. doi:10.1098/rspa.1971.0141.

Linares, A.V., Vandevelde, F., Pantigny, J., Falcimaigne-Cordin, A., Haupt, K., 2009. Polymer films composed of surface-bound nanofilaments with a high aspect ratio, molecularly imprinted with small molecules and proteins. Adv. Funct. Mater. 19, 1299–1303. doi:10.1002/adfm.200801222.

Lindström, S.B., Vader, D.A., Kulachenko, A., Weitz, D.A., 2010. Biopolymer network geometries: characterization, regeneration, and elastic properties. Phys. Rev. E Stat. Nonlinear Soft Matter Phys. 82, 051905. doi:10.1103/PhysRevE.82.051905.

Liu, J., Rinzler, A.G., Dai, H., Hafner, J.H., Bradley, R.K., Boul, P.J., Lu, A., Iverson, T., Shelimov, K., Huffman, C.B., Rodriguez-Macias, F., Shon, Y.-S., Lee, T.R., Colbert, D.T., Smalley, R.E., 1998. Fullerene pipes. Science 280, 1253–1256.

Lu, J.P., 1997. Elastic properties of carbon nanotubes and nanoropes. Phys. Rev. Lett. 79, 1297–1300. doi:10.1103/PhysRevLett.79.1297.

Maxwell, J.C., 1864. On reciprocal figures and diagrams of forces. London Edinburgh Dublin Philos. Mag. J. Sci. 27, 250–261. doi:10.1080/14786446408643663.

Persson, B.N.J., 2006. Contact mechanics for randomly rough surfaces. Surf. Sci. Rep. 61, 201–227. doi:10.1016/j.surfrep.2006.04.001.

Picu, R.C., 2011. Mechanics of random fiber networks—a review. Soft Matter 7, 6768. doi:10.1039/c1sm05022b.

Picu, R.C., Sengab, A., 2018. Structural evolution and stability of non-crosslinked fiber networks with inter-fiber adhesion. Soft Matter 14, 2254–2266. doi:10.1039/C7SM02555F.

Picu, R.C., Subramanian, G., 2011. Correlated heterogeneous deformation of entangled fiber networks. Phys. Rev. E 84, 031904. doi:10.1103/PhysRevE.84.031904.

Schmied, F.J., Teichert, C., Kappel, L., Hirn, U., Schennach, R., 2012. Joint strength measurements of individual fiber-fiber bonds: an atomic force microscopy based method. Rev. Sci. Instrum. 83, 073902. doi:10.1063/1.4731010.

Sengab, A., Picu, R.C., 2018. Filamentary structures that self-organize due to adhesion. Phys. Rev. E 97, 032506. doi:10.1103/PhysRevE.97.032506.

Shahsavari, A.S., Picu, R.C., 2013. Elasticity of sparsely cross-linked random fibre networks. Philos. Mag. Lett. 93, 356–361. doi:10.1080/09500839.2013.783241.

Streichfuss, M., Erbs, F., Uhrig, K., Kurre, R., Clemen, A.E.M., Böhm, C.H.J., Haraszti, T., Spatz, J.P., 2011. Measuring forces between two single actin filaments during bundle formation. Nano Lett. 11, 3676–3680. doi:10.1021/nl201630y.

Style, R.W., Jagota, A., Hui, C.-Y., Dufresne, E.R., 2017. Elastocapillarity: surface tension and the mechanics of soft solids. Annu. Rev. Condens. Matter Phys. 8, 99–118. doi:10.1146/annurev-conmatphys-031016-025326.

Tabor, D., 1977. Surface forces and surface interactions. J. Colloid Interface Sci. 58, 2–13. doi:10.1016/0021-9797(77)90366-6.

Tempel, M., Isenberg, G., Sackmann, E., 1996. Temperature-induced sol-gel transition and microgel formation in α-actinin cross-linked actin networks: a rheological study. Phys. Rev. E 54, 1802–1810. doi:10.1103/PhysRevE.54.1802.

Toll, S., 1998. Packing mechanics of fiber reinforcements. Polym. Eng. Sci. 38, 1337–1350. doi:10.1002/pen.10304.

Yunoki, S., Hatayama, H., Ebisawa, M., Kondo, E., Yasuda, K., 2015. A novel fabrication method to create a thick collagen bundle composed of uniaxially aligned fibrils: an essential technology for the development of artificial tendon/ligament matrices. J. Biomed. Mater. Res. Part A 103, 3054–3065. doi:10.1002/jbm.a.35440.

Žagar, G., Onck, P.R., Van Der Giessen, E., 2015. Two fundamental mechanisms govern the stiffening of cross-linked networks. Biophys. J. 108, 1470–1479. doi:10.1016/j.bpj.2015.02.015.

Zilman, A.G., Safran, S.A., 2003. Role of cross-links in bundle formation, phase separation and gelation of long filaments. Europhys. Lett. 63, 139–145. doi:10.1209/epl/i2003-00489-5.